International Journal of Thermal Sciences 101 (2016) 9–23

Contents lists available at ScienceDirect

International Journal of Thermal Sciences

journal homepage: www.elsevier.com/locate/ijts

DSMC and R13 modeling of the adiabatic surface

Alireza Mohammadzadeh*, Anirudh Rana, Henning Struchtrup

Department of Mechanical Engineering, University of Victoria, Victoria, British Columbia, Canada

ARTICLE INFO

Article history:
Received 19 March 2015
Received in revised form
2 October 2015
Accepted 4 October 2015
Available online xxx

Keywords:
Kinetic theory
DSMC
R13
Boundary condition
Adiabatic surface

ABSTRACT

Adiabatic wall boundary conditions for rarefied gas flows are described with the isotropic scattering model. An appropriate sampling technique for the direct simulation Monte Carlo (DSMC) method is presented, and the corresponding macroscopic boundary equations for the regularized 13-moment system (R13) are obtained. DSMC simulation of a lid driven cavity shows slip at the wall, which, as a viscous effect, creates heat that enters the gas while there is no heat flux in the wall. Analysis with the macroscopic equations and their boundary conditions reveals that this heat flux is due to viscous slip heating, and is the product of slip velocity and shear stress at the adiabatic surface. DSMC simulations of the driven cavity with adiabatic walls are compared to R13 simulations, which both show this non-linear effect in good agreement for Kn < 0.3.

1. Introduction

Significant reduction in size of electro mechanical systems extends the demands for modeling and interpreting the flow behavior of gasses to micro scales. As the mean free path λ, i. e., the average distance that a molecule travels between collisions becomes comparable with the flow length scale, L, the theoretical assumption in the conventional constitutive relations, i.e., the laws of Navier–-Stokes and Fourier, lose their validity. The Knudsen number, which is the ratio of the mean free path to the characteristic length of the flow domain, $\mathrm{Kn} = \frac{\lambda}{L}$, is the main indicator of the degree of rarefaction in gases.

The Boltzmann equation describes the behavior of a gas flow at every degree of rarefaction [1]. However, due to the six dimensional phase space and the complexity associated with the molecular collision term, solving the Boltzmann equation is challenging, and numerically expensive. Some researchers propose to solve kinetic model equations using deterministic numerical schemes [2,3]. These model equations have the same main characteristics as the Boltzmann equation, but avoid some of the complexity arising due to the collision term.

Another method to approximate the Boltzmann equation, is to derive a set of macroscopic transport equations which can describe the flow behavior to various degrees of accuracy. The Grad moment method [4] extends the set of conventional hydrodynamic variables, such as, density, temperature, and velocity, by introducing stress, heat flux, and other higher moments. However, due to the hyperbolic nature, the Grad moment equations exhibit un-physical subshocks [5,6].

The regularized 13 moments (R13) equations are derived by combining elements of the Grad and Chapman-Enskog methods, utilizing the concept of order of magnitude in the Knudsen number [7,8]. The R13 equations are stable [9], accurate up to the third order in terms of Knudsen number, and benefit from a complete set of boundary conditions [10,11].

Alternatively, the Boltzmann equation can be solved by stochastic schemes, commonly known as direct simulation Monte Carlo (DSMC). The DSMC method, first proposed by Bird [12], is a particle based microscopic method that converges to the solution of Boltzmann equation in the limit of infinite simulating particles [13]. In this method, simulating particles represent a cloud of gas molecules that travel and collide with each other and solid surfaces. The macroscopic properties of the gas, such as temperature, shear stress or heat flux are obtained by taking the appropriate average of microscopic properties of simulating particles.

According to Maxwell's original paper [14], when the surface is microscopically rough *and* the incident molecules are performing multiple scattering, *or* are momentarily trapped *or* absorbed on the surface, we can expect the surface to behave as a diffusive reflector. However, it is well known from experiments on molecular beams that diffusive reflection typically does *not* occur. Instead, beams are reflected in plumes that center on the reflection direction [1,15]. To

* Corresponding author.
E-mail address: alirezam@uvic.ca (A. Mohammadzadeh).

http://dx.doi.org/10.1016/j.ijthermalsci.2015.10.007
1290-0729/

at least have some elements of the plume, Maxwell amended his model by the possibility for specular reflection.

As listed in [12], the diffusive reflection law should be critically reviewed when one or more of the following factors are present:

- The ratio of the molecular weight of the gas to the surface molecules is small in comparison with unity.
- Or the translational energy of the molecules relative to the surface is larger than several electron volts.
- A smooth metal surface that has been outgassed through exposure to high vacuum and high temperature.

In the current study, we model a rarefied gas of light atoms enclosed in a cavity with heavy surface molecules. In the collision, the (light) gas particle has little change of absolute kinetic energy, while its collision angle depends on the detailed microscopic geometry of collision with the (heavy) surface atom.

The conventional assumptions for the diffuse surface cannot be employed here. At such a surface, particles thermalize with the wall, and leave in a Maxwell distribution– that is accompanied by marked exchanged between gas particle and the wall. The Maxwell model would allow the description of non-diffusive collisions only by accounting for more specular reflections. However, specular reflection are not expected, since the surface is never flat-on the microscopic level. Moreover, specularly reflecting walls exchange neither energy nor momentum, hence there is no shear force on the gas.

Modeling particles reflecting from a surface with a defined temperature is straightforward [12]; however, in the case of an adiabatic surface, assigning a velocity to the reflecting particle from a wall with unknown temperature becomes non-trivial. Researchers have proposed various methods to implement the adiabatic boundary condition in the DSMC method. Wang et al. [16,17] introduced the inverse temperature sampling technique to heat flux on the wall. More recently, Akhlaghi et al. [18] proposed an iterative scheme to impose the heat flux boundary condition in DSMC method. In this scheme, an estimate to the wall temperature is initially made. Then, as the solution evolves in time, the wall temperature is modified according to the predicted heat flux associated with the assumed temperature. They showed that by using the Maxwell model and adjusting the wall temperature iteratively, one can make the energy flux through a surface vanish, i.e., model an adiabatic Maxwell surface. Tzeng et al. [19], proposed a microscopic method to model the adiabatic surface. In this model the normal component of the velocity is reversed, while the two other planar components are obtained by using a single random number, such that the magnitude of velocity vector remains unchanged in the collision. Although this microscopic treatment leads to zero energy transfer through the surface, the use of normal velocity reversal in this model seems not necessary true for the particles colliding with a rough wall.

In the current study the isotropic scattering kernel [20] is utilized to model the adiabatic surface in the DSMC method and R13 equations. Here, the *no energy transfer* condition is directly imposed on each particle colliding with the adiabatic surface. This method is expected to be fast and more accurate in convergence of the DSMC solution compared to the iterative schemes. The appropriate sampling technique in the DSMC method is presented, and the corresponding boundary equations for the R13 equations are derived. Then we briefly discuss the steps required to model an adiabatic Maxwell surface using the macroscopic approach, and show the agreement between the macroscopic boundary conditions obtained from the adiabatic Maxwell model, and the isotropic scattering model for the R13 equations. Using the obtained boundary conditions, the DSMC and R13 equations are utilized to model a partly adiabatic cavity in the rarefaction regime. The DSMC results show that the heat flux profile has a component normal to the adiabatic surface. This generated heat is well captured by the R13 equations, which allows us to interpret it as the viscous slip heating in the boundary of the adiabatic surface. Indeed, the heat flow into the gas is the product of shear stress and slip velocity.

The remainder of the paper is organized as follows. The solution methods utilized in this study are introduced in Section 2. In Section 3 the boundary condition to model an adiabatic surface using the isotropic scattering kernel is described, then in Section 3.3 the microscopic approach for modeling the adiabatic surface in the DSMC is introduced. The associated macroscopic boundary conditions for the R13 equations are derived in Section 3.4. The adiabatic Maxwell surface is presented in Section 3.5, and the appropriate wall temperature is introduced. Afterwards, in Section 4 the proposed boundary conditions are utilized to perform a microscopic and macroscopic modeling of the partly adiabatic lid driven cavity, and the obtained results are discussed. The paper ends with our conclusions in Section 5.

2. Governing equation and method of solution

2.1. Distribution function and Boltzmann equation

In kinetic theory a gas is described by the density distribution function $f(t, x_i, c_i)$ such that $f d\mathbf{x} d\mathbf{c}$ denotes the number of particles in the phase space element $d\mathbf{x}d\mathbf{c}$ at time t. The Boltzmann equation describes the evolution of the density distribution function in phase space ($\mathbf{x}$, $\mathbf{c}$) by accounting for the translational motion and collisions of the particles in the gas, as

$$\frac{\partial f}{\partial t} + c_k \frac{\partial f}{\partial x_k} + G_k \frac{\partial f}{\partial c_k} = \mathscr{J}(f,f), \tag{1}$$

where G_k is the external force acting on the gas. The term $\mathscr{J}(f,f)$ is the collision operator that describes the change of the distribution function due to interaction between particles.

Macroscopic quantities such as mass density ρ, velocity v_i, temperature T, shear stress σ_{ij} and heat flux q_i are moments of the distribution function, obtained by integration over velocity space $\mathbf{c}$,

$$\begin{aligned} &\rho = m\int f d\mathbf{c}, \quad v_i = \frac{m}{\rho}\int c_i f d\mathbf{c}, \quad 3RT = \frac{m}{\rho}\int C^2 f d\mathbf{c}, \\ &\sigma_{ij} = m\int C_{<i}C_{j>} f d\mathbf{c}, \quad 2q_i = m\int C_i C^2 f d\mathbf{c}. \end{aligned} \tag{2}$$

Here, m is the mass of particle, R is the specific gas constant and $C_i = c_i - v_i$ is the peculiar velocity of the gas particles.

A rarefied gas is well described by the Boltzmann equation for all Knudsen numbers. However, the Boltzmann equation is difficult to solve deterministically due to six dimensional phase space description, as well as the non-linearity in the collision term.

2.2. DSMC method (microscopic method)

The DSMC method is a statistical method, based on the kinetic theory of dilute gases, to model rarefied gas flows [12]. In this method, many independent simulating particles are used to model gaseous flows, where each particle represents a large number of real gas molecules. In the DSMC method the simulating particles are allowed to move and collide; however, the motion and collision of the particles are assumed to be decoupled. The time step is chosen as a fraction of the mean collision time to ensure pure motion in the elapsed movement time. In order to implement DSMC, the flow domain must be divided into computational cells.

The cell size is chosen small enough to ensure small changes in the thermodynamic properties of the flow across each cell. To satisfy the cell size limitation in the current study, the mesh size in both directions of the square domain is chosen as 0.1λ. Within each cell, the macroscopic thermodynamic properties are sampled from molecular properties. Moreover, in each time step, only the particles within a computational cell are allowed to perform collisions. For the sake of accuracy, the cells are divided into sub-cells to facilitate the selection of collision pairs. The no-time-counter (NTC) method is used to choose the collision pairs in each computational cell, therefore the computational time is proportional to the number of the simulating particles [12]. Later on, we will compare DSMC results with extended macroscopic R13 equations, which are more conventional for Maxwell molecules. Therefore, in the current study, the code of Roohi and co-workers [21–25] is modified to model Maxwell molecules in a cavity with adiabatic and diabatic walls. The fluid is argon as a Maxwell gas, with $m = 6.63 \times 10^{-26}$ kg and a reference viscosity of $\mu_0 = 1.9549 \times 10^{-5}$Pa·s. In order to relate the particle diameter, d, to the reference viscosity we used the relation [12].

$$d^2 = \frac{5(\alpha+1)(\alpha+2)\sqrt{mkT_0/\pi}}{4\alpha(5-2\omega)(7-2\omega)\mu_0}.$$

Here, k and m are, respectively, the Boltzmann constant and the molecular mass for the gas, and T_0 is the reference temperature. In order to model Maxwell molecules we set $\alpha = 2.13986$ and $\omega = 1$ [12]. Following [12], the Knudsen number is obtained as

$$\mathrm{Kn}_b = \frac{1}{L}\frac{1}{\sqrt{2}\pi d^2 n_0},$$

where n_0 is the reference number density. Another definition of the Knudsen number is based on the viscosity [26].

$$\mathrm{Kn} = \frac{\mu_0}{\rho_0\sqrt{\mathrm{R}T_0}L} \cong 1.27\mathrm{Kn_b}. \tag{3}$$

Here, ρ_0 is the reference density. This definition of the Knudsen number, Kn, is related to Bird's definition of Knudsen number, $\mathrm{Kn_b}$, for the Maxwell molecules as above. To avoid confusion, all results presented in this article are given in terms of the Knudsen number Kn in Eq. (3). The DSMC simulation starts with 32 particles located in each cell. As the flow reaches the steady state, the molecular properties are sampled over a large period of time to reduce the statistical scattering. In addition, a filtering post processor is used to minimize the scattering in the predicted results of thermodynamic properties. In this filtering, the sampled macroscopic properties, F, in cell N are averaged over a pattern of its neighboring cells, see [23],

$$\widetilde{F}_{(N)} = \frac{F_N + \sum_{I=1}^{I=N_n} F_I}{N_n + 1}.$$

2.3. R13/NSF equations (macroscopic models)

The detailed derivation of the R13 equations from the Boltzmann equation can be found in [9,27]; here we only present the final equations. Both macroscopic models consist of the conservation laws for mass, momentum, and energy,

$$\frac{D\rho}{Dt} + \rho\frac{\partial v_k}{\partial x_k} = 0, \tag{4a}$$

$$\rho\frac{Dv_i}{Dt} + \frac{\partial p}{\partial x_i} + \frac{\partial \sigma_{ik}}{\partial x_k} = \rho G_i, \tag{4b}$$

$$\frac{3}{2}\rho\frac{D\theta}{Dt} + (p\delta_{ij} + \sigma_{ij})\frac{\partial v_i}{\partial x_j} + \frac{\partial q_k}{\partial x_k} = 0. \tag{4c}$$

Here, the pressure p obeys the ideal gases law, $p = \rho RT = \rho\theta$. Closure of the conservation laws (4a–4c) requires specification of the stress tensor, σ_{ik}, and the heat flux vector, q_k, as constitutive equations. In classical hydrodynamics, the NSF equations provide these constitutive relations from the laws of Fourier heat transfer and the Navier–Stokes relation for the stress, as

$$q_i = -\frac{15}{4}\mu\frac{\partial\theta}{\partial x_i}, \quad \sigma_{ij} = -2\mu\frac{\partial v_{\langle i}}{\partial x_{j\rangle}}. \tag{5}$$

The indices inside angular brackets denote the symmetric trace-free part of tensors [26].

In extended hydrodynamics theory, however, stress and heat–flux follow full balance equations as [26,28,29].

$$\frac{D\sigma_{ij}}{Dt} + \frac{4}{5}\frac{\partial q_{\langle i}}{\partial x_{j\rangle}} + \sigma_{ij}\frac{\partial v_k}{\partial x_k} + 2\sigma_{k\langle i}\frac{\partial v_{j\rangle}}{\partial x_k} + \frac{\partial m_{ijk}}{\partial x_k} = -2\rho\theta\frac{\partial v_{\langle i}}{\partial x_{j\rangle}} - \frac{\rho\theta}{\mu}\sigma_{ij}, \tag{6}$$

$$\frac{Dq_i}{Dt} + \frac{5}{2}\sigma_{ik}\frac{\partial\theta}{\partial x_k} - \frac{\theta\sigma_{ik}}{\rho}\frac{\partial\rho}{\partial x_k} - \frac{\sigma_{ik}}{\rho}\frac{\partial\sigma_{kl}}{\partial x_l} + \theta\frac{\partial\sigma_{ik}}{\partial x_k} + \frac{7}{5}\left(q_k\frac{\partial v_i}{\partial x_k} + q_i\frac{\partial v_k}{\partial x_k}\right) + \frac{2}{5}q_k\frac{\partial v_k}{\partial x_i} + \frac{1}{6}\frac{\partial\Delta}{\partial x_i} + \frac{1}{2}\frac{\partial R_{ik}}{\partial x_k} + m_{ijk}\frac{\partial v_j}{\partial x_k} = -\frac{5}{2}\rho\theta\frac{\partial\theta}{\partial x_i} - \mathrm{Pr}\frac{\rho\theta}{\mu}q_i, \tag{7}$$

where Pr is the Prandtl number, which is 2/3 for Maxwell molecules, and close to 2/3 for other molecule types. The coefficients (4/5, 1, 2, …, Pr) are valid for Maxwell molecules. Some of the coefficients change with the molecule types more significantly (up to 20%). The R13 equations for other molecule types were derived in [8], where the method is outlined and coefficients are given for hard sphere molecules. Also for other molecule types, the R13 equations are of third order of accuracy in terms of Knudsen number. Here we are more interested in the modelling of the adiabatic surface, and used the R13 equations in their most convenient form, which is for Maxwell molecules. The modelling of the adiabatic surface can be extended to all molecule types. In Eqs. (6 and 7) the higher moments m_{ijk}, Δ,R_{ij}, appear as unknown fluxes. Grad's original closure in [4] gives $\Delta = R_{ij} = m_{ijk} = 0$, while in the R13 equations these quantities are obtained as [11,27]

$$\begin{aligned}
\Delta &= 5\frac{\sigma_{kl}\sigma_{kl}}{\rho} + \frac{56}{5}\frac{q_k q_k}{p} - 12\mu\left(\theta\frac{\partial(q_k/p)}{\partial x_k}\right),\\
R_{ij} &= \frac{20}{7}\frac{\sigma_{k\langle i}\sigma_{j\rangle k}}{\rho} + \frac{192}{75}\frac{q_{\langle i}q_{j\rangle}}{p} - \frac{24}{5}\mu\left(\theta\frac{\partial\left(q_{\langle i}/p\right)}{\partial x_{j\rangle}}\right),\\
m_{ijk} &= \frac{20}{15}\frac{q_{\langle i}\sigma_{jk\rangle}}{p} - 2\mu\left(\theta\frac{\partial(\sigma_{\langle ij}/p)}{\partial x_{k\rangle}}\right).
\end{aligned} \tag{8}$$

A Chapman-Enskog expansion of Eqs. (6) and (7) shows that the R13 equations are of third order accuracy in the Knudsen number [9,26].

3. Boundary conditions

The boundary conditions describe the interaction between the gas molecules and the surface. In kinetic theory this is done by prescribing the velocity probability density of the molecules after hitting the wall. Since the actual microscopic interaction between gas particles and a solid boundary is quite complicated, it is common to use simplified models. Many gas–surface interaction models have been proposed [1]. The Maxwell accommodation model is the one most widely used as the boundary condition for the Boltzmann equation [1,26,30] and in DSMC simulations [12], which assumes particles are either thermalized with the surface or specularly reflected.

3.1. Dynamics of gas–surface interaction

When the surface is microscopically rough and the mass ratio of gas particle and surface particle is close to unity, the gas particles might be trapped and perform multiple collisions with the surface to thermalize with the wall [12]. In this case the surface is behaving as a diffusive reflector. However, when the mass ratio of gas and surface particle is not close to unity, the assumption of the diffusive reflection must be critically reviewed [12].

Figure 1-a shows a light gas particle of mass m_α and velocity $\mathbf{c}'_\alpha$ colliding with a heavy surface particle of mass m_β and velocity $\mathbf{c}'_\beta$. Using the dynamics of collision [29] to obtain the post collision velocities, $\mathbf{c}_\alpha$ and $\mathbf{c}_\beta$, we have

$$\mathbf{c}_\alpha = \mathbf{c}'_\alpha + 2\frac{m_\beta}{m_\alpha + m_\beta}\mathbf{K}^{\beta\alpha}\left(\mathbf{K}^{\beta\alpha}\cdot\mathbf{g}'^{\beta\alpha}\right),$$

$$\mathbf{c}_\beta = \mathbf{c}'_\beta - 2\frac{m_\alpha}{m_\alpha + m_\beta}\mathbf{K}^{\beta\alpha}\left(\mathbf{K}^{\beta\alpha}\cdot\mathbf{g}'^{\beta\alpha}\right).$$

Here, $\mathbf{K}^{\beta a}$ is the apsidal vector, defined as [29]

$$\mathbf{K}^{\beta\alpha} = \frac{\mathbf{g}'^{\beta\alpha} - \mathbf{g}^{\beta\alpha}}{|\mathbf{g}'^{\beta\alpha} - \mathbf{g}^{\beta\alpha}|}.$$

The relative velocities before and after collision are

$$\mathbf{g}'^{\beta\alpha} = \mathbf{c}'_\beta - \mathbf{c}'_\alpha \quad \text{and} \quad \mathbf{g}^{\beta\alpha} = \mathbf{c}_\beta - \mathbf{c}_\alpha.$$

Since there is a large difference between the masses, $m_\alpha \ll m_\beta$, we have

$$\frac{m_\alpha}{m_\alpha + m_\beta} = \varepsilon, \quad \frac{m_\beta}{m_\alpha + m_\beta} = 1 - \varepsilon,$$

where $\varepsilon \ll 1$. Assuming that the surface is stationary, the average velocity of the surface particle is zero $\overline{\mathbf{c}'_\beta} = 0$. Therefore, in average, the relative velocity before collision is $\mathbf{g}'^{\beta\alpha} = -\mathbf{c}'_\alpha$. The post collision velocity of the light particle simplifies to

$$\mathbf{c}_\alpha = \left(\mathbf{I} - 2(1-\varepsilon)\mathbf{K}^{\beta\alpha}\mathbf{K}^{\beta\alpha}\right)\cdot\mathbf{c}'_\alpha, \tag{9}$$

where $\mathbf{I}$ is the unit tensor. In order to obtain the magnitude of post collision velocity of the light particle, we multiply both sides of Eq. (9) with $\mathbf{c}_\alpha$ to get

$$|\mathbf{c}_\alpha|^2 = \left[\delta_{jk} + 4\left(\varepsilon^2 - \varepsilon\right)K_j^{\beta\alpha}K_k^{\beta\alpha}\right]c'_{j\alpha}c'_{k\alpha}. \tag{10}$$

Note that in Eq. (10), we used $K_i^{\beta\alpha}K_i^{\beta\alpha} = 1$. By assuming a very small value for ε we have

$$|\mathbf{c}_\alpha| \simeq |\mathbf{c}'_\alpha|.$$

Therefore, as a result of the collision between a very light gas particle and a heavy wall particle, the light gas particle will be reflected with almost the same kinetic energy, which subsequently leads to very small thermal accommodation. Thomas [31] reported that the thermal accommodation coefficient becomes significantly less than unity, when the mass ratio of gas particle and surface particle in the experiment is small. The momentum exchange between the gas and surface leads to a different reflection direction for the gas particle, which is dependent on the detailed microscopic geometry of collision with the surface. Figure 1-b demonstrates the collision between two particles in the plane of the relative velocities with the apsidal vector $\mathbf{K}$. For a rough surface as in Fig. 1-a, it is expected that the reflected particle has no preferred direction. All possible reflection directions will have the same likelihood, that is the direction will be isotropically distributed.

3.2. Adiabatic surface model (isotropic scattering)

The adiabatic boundary condition implies no-energy-transfer through the surface, where energy is conserved for each individual particle. The total transport of energy through a wall with the normal in n-direction, as seen in the rest frame of the wall, can be written as

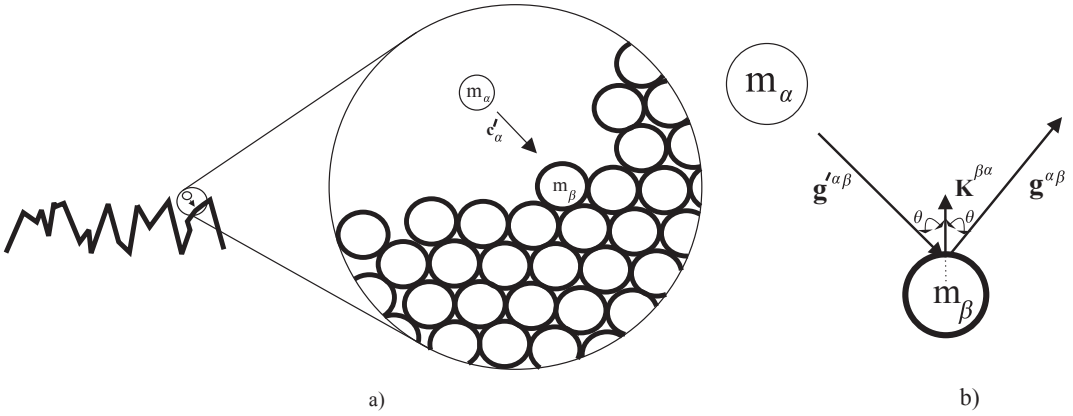

Fig. 1. Gas and rough surface interaction at the molecular level, a) Collision of a light gas particle with a heavy surface particle, b) Dynamics of collision on the relative velocities plane when $\frac{m_\alpha}{m_\beta} \ll 1$.

$$U_n = m\int c_n^W \frac{(c^W)^2}{2} f d\mathbf{c} = q_n + \sigma_{tn}\mathscr{V}_t + \mathscr{V}_n\left(\frac{1}{2}\rho\mathscr{V}^2 + \frac{5}{2}\rho RT\right),$$

where $c_i^W = c_i - v_i^W$ is the particle velocity in the rest frame of the wall, and $\mathscr{V}_t = v_t - v_t^W$ is the tangential slip velocity. At a non-accumulating, adiabatic surface at rest we have $v_i^W = v_n = e_n = 0$, therefore,

$$q_n = -\mathscr{V}_t\sigma_{tn}. \tag{11}$$

From Eq. (11) we can see that, while the overall energy flux vanishes, there is a non-convective heat flux q_n, which transfers the heat of slip friction, $-\mathscr{V}_t\sigma_{tn}$, into the gas. We denote this effect as *viscous slip heating*; A detailed discussion will follow in the sequel.

We are interested in adiabatic surfaces with friction. These cannot be described by the pure specular Maxwell model, where an adiabatic wall is necessarily frictionless. An adiabatic surface can be modeled utilizing the fully diffusive Maxwell surface, if the wall temperature is adjusted in each surface element so that the macroscopic heat flux follows from Eq. (11). This model, however, requires an iterative scheme to modify the microscopic boundary conditions in the DSMC method. In the macroscopic method, on the other hand, this process is rather straightforward and we will be further discussed in Section 3.5.

We now turn our attention to processes where the particles leaving the surface are isotropically reflected while the magnitude of their velocities is that of the incoming particle. Thus, the collision with the surface does not change the kinetic energy of the individual particle, so that the surface is adiabatic in the rest frame of the wall. Some particles exchange momentum with the wall so that there is friction on the surface [20,32].

Accordingly, the phase density of the particles in an infinitesimal neighborhood of the wall is

$$\bar{f} = \begin{cases} f^*\left(c_i^W, x_i, t\right), & c_k^W n_k \geq 0 \\ f\left(c_i^W, x_i, t\right) & c_k^W n_k \leq 0. \end{cases} \tag{12}$$

Here, f^* in (12) denotes the phase density of particles leaving the wall ($c_k^W n_k \geq 0$). The function f^* must be chosen such that the wall does not accumulate particles, it must be isotropic in velocity, i.e.,

$$f^*\left(c_i^W, x_i, t\right) = f^*\left(\left|c^W\right|, x_i, t\right). \tag{13}$$

It is convenient to introduce spherical coordinates $\{|c^W|, \vartheta, \phi\}$ for the velocity space, i.e., with the direction vector ξ_i,

$$c_i^W = \left|c^W\right|\xi_i = \left|c^W\right|\{\sin\vartheta\cos\phi, \quad \sin\vartheta\sin\phi, \quad \cos\vartheta\}_i,$$

where $|c^W| \in [0,\infty]$, $\vartheta \in [0,\pi]$, $\phi \in [0, 2\pi]$, and $d\Omega = \sin\vartheta d\vartheta d\phi$. Writing the conservation of the normal number flux of the gas to the wall with the assumption of isotropic distribution function, Eq. (13), gives

$$f^*\left(\left|c^W\right|\right) = \frac{\int_{\pi/2}^{\pi}\int_0^{2\pi} c_k n_k f \sin\vartheta d\phi d\vartheta}{\int_{\pi/2}^{\pi}\int_0^{2\pi} c_k n_k \sin\vartheta d\phi d\vartheta}. \tag{14}$$

3.3. Microscopic boundary conditions for adiabatic surface in the DSMC

Boundary conditions in the DSMC method is expressed by specifying the velocity vector for particles reflecting from the surface. For this means, first the distribution function for the reflecting particles is specified, and then the velocity vector is derived by sampling from this distribution function.

In the DSMC method changes in the total energy of a particle due to the collision with a solid surface determines the amount of energy that flows through the wall. Since monatomic particles only have translational energy, implementing the adiabatic boundary condition on a surface is equivalent to requiring an equal amount of translational energy before and after collision with the surface. For a particle colliding with a surface, the translational energy before collision is

$$U' = \frac{1}{2}m\left(c_x'^2 + c_y'^2 + c_z'^2\right) = \frac{1}{2}mc'^2,$$

where m is the particle mass, and the apostrophe denotes the molecular state before the collision. As a particle reflects from the adiabatic surface, the velocity vector must have the same magnitude, but different direction. Assuming that the particles have the isotropic probability for scattering in all directions, the scattering kernel $P(\mathbf{c}' \rightarrow \mathbf{c})$ for a particle reflecting from a surface with the normal in the $y-$ direction is [20]

$$P(\mathbf{c}' \rightarrow \mathbf{c}) = \frac{1}{\pi c^3} c_y \delta(c' - c).$$

Here, $\mathbf{c}$ is the particle velocity vector after collision with the surface. Sampling requires the cumulative probabilities, which are best defined based on spherical coordinates $\{c, \theta, \phi\}$ so that

$$\begin{aligned} P(\mathbf{c}' \rightarrow \mathbf{c})d\mathbf{c} &= \frac{1}{\pi c^3} c\cos\phi\,\delta(c' - c)c^2 dc \sin\phi d\phi d\theta \\ &= [\delta(c' - c)dc]\left[\frac{1}{2\pi}d\theta\right][2\cos\phi\sin\phi d\phi]. \end{aligned} \tag{15}$$

The delta function indicates that the absolute velocity of the leaving particle is deterministic, $c = c'$. However, the direction of the leaving particle is subject to the process of random isotropic scattering. By considering the cumulative probabilities we obtain

$$F_\theta = \int_0^{\Theta}\frac{1}{2\pi}d\theta, \quad F_\phi = \int_0^{\Phi} 2\cos\phi\sin\phi d\phi.$$

Here, Θ, Φ are the angles for the particles leaving. The integrals for the cumulative probabilities F_θ, F_ϕ can be solved analytically to give

$$\Theta = 2\pi F_\theta, \tag{16}$$

$$\Phi = \arcsin\left(\sqrt{F_\phi}\right) \tag{17}$$

By converting back to Cartesian coordinates, and noting that $\cos(\arcsin(x)) = \sqrt{1 - x^2}$, the velocity of the randomly scattered particle is

$$\begin{aligned} c_x &= c'\sqrt{F_\phi}\cos(2\pi F_\theta), \\ c_y &= c'\sqrt{1 - F_\phi}, \\ c_z &= c'\sqrt{F_\phi}\sin(2\pi F_\theta). \end{aligned} \tag{18}$$

Using this method, particles hitting the surface are reflected into arbitrary directions while carrying the same translational energy as before the collision.

It is also worth noting that by following the same methodology we can model an adiabatic moving surface in DSMC. The observer on the wall frame, which moves with the velocity of $\mathbf{V}_W$, measures the incoming particle's velocity as

$$\mathbf{c}'^W = \mathbf{c}' - \mathbf{V}_W.$$

The components of the reflecting velocity vector, still in the rest frame of the wall, are obtained as

$$c_x^W = c'^W\sqrt{F_\phi}\cos(2\pi F_\theta),$$
$$c_y^W = c'^W\sqrt{1-F_\phi},$$
$$c_z^W = c'^W\sqrt{F_\phi}\sin(2\pi F_\theta).$$

Finally, the velocity of the reflecting particle in the rest frame is $\mathbf{c} = \mathbf{c}^W + \mathbf{V}_W$.

3.4. Macroscopic boundary conditions for adiabatic surface in R13/NSF equations

To find the macroscopic boundary conditions, we follow the method outlined in Refs. [4,11]. We consider the continuity of normal fluxes over an infinitesimal surface area element which gives

$$m\int \Psi_A c_k^W n_k f\, d\mathbf{c}^W = m\int \Psi_A c_k^W n_k \bar{f}\, d\mathbf{c}^W, \tag{19}$$

where Ψ_A are polynomials of the particle velocity, c_i^W. Integrating (19) yields relations between the moments in the gas and the wall properties (θ_W, v_i^W) that serve as boundary conditions for the moments.

To perform the integrations in Eq. (19), the velocity distribution function f and the appropriate velocity functions Ψ_A are required. For the R13 system, the phase density in the gas is approximated by a Grad-type distribution that reads [26]

$$f_{R13} = f_M(1+\Phi), \tag{20}$$

where f_M denotes the local Maxwellian and

$$\Phi = \left(\frac{1}{8} - \frac{C^2}{12\theta} + \frac{C^4}{120\theta^2}\right)\frac{\Delta}{\rho\theta^2} + \frac{C_iC_j}{2\rho\theta^2}\sigma_{ij} - \frac{1}{\rho\theta^2}\left(1-\frac{C^2}{5\theta}\right)C_jq_j + \frac{C_iC_jC_k}{6\rho\theta^3}m_{ijk} - \frac{1}{4\rho\theta^3}\left(1-\frac{C^2}{7\theta}\right)C_iC_jR_{ij}.$$

Here, $C_k = c_k^W - (v_k - v_k^W)$ is the peculiar velocity (i.e., the velocity in the rest frame of the gas), with $C_kn_k = c_k^Wn_k$.

Grad observed that, in order to get meaningful boundary conditions, the velocity functions Ψ_A must be even in the normal component of the particle velocity $c_k^Wn_k$ [4]. For example, if we consider a surface with the normal in $y-$ direction ($y = x_2$), we take

$$\Psi_A = \left\{1, C_x, C^2, C_yC_y, C_xC_x, C^2C_x\right\}, \tag{21}$$

which correspond to the fluxes

$$m\int \Psi_A c_k^W n_k f d\mathbf{c} = \left\{\rho v_y, \sigma_{xy}, q_y, m_{yyy}, m_{xxy}, R_{xy}\right\}. \tag{22}$$

Using the isotropic distribution function for the reflecting particles, Eq. (12), and performing the integrations for Eq. (19), we obtain the boundary conditions

$$\begin{aligned}
&v_y = 0,\\
&\sigma_{xy} = \sqrt{\frac{2}{\pi\theta}}\left(-\frac{1}{2}m_{xyy} - \frac{1}{5}q_x - P\mathscr{V}_x\right)n_y,\\
&q_y = -\sigma_{xy}\mathscr{V}_x,\\
&R_{xy} = 11\theta\sigma_{xy} + \sqrt{\frac{2}{\pi\theta}}\left(36\theta\mathscr{V}_x\left(P - \frac{2}{3}\rho\theta - \frac{3}{8}\sigma_{yy} + \frac{1}{112}\frac{R_{yy}}{\theta}\right) + 5\theta m_{xyy}\right)n_y,\\
&m_{xxy} = -\frac{1}{10}\sigma_{xy}\mathscr{V}_x + \sqrt{\frac{2}{\pi\theta}}\left(\frac{3}{2}\mathscr{V}_x^2\left(P - \frac{1}{2}\rho\theta\right) - \theta\left(\sigma_{xx} - \frac{1}{4}\sigma_{yy}\right) - \frac{1}{14}R_{xx} + \frac{1}{56}R_{yy}\right)n_y,\\
&m_{yyy} = \frac{1}{5}\sigma_{xy}\mathscr{V}_x + \sqrt{\frac{2}{\pi\theta}}\left(-\mathscr{V}_x^2\left(P - \frac{1}{2}\rho\theta\right) - \frac{3}{28}R_{yy} - \frac{3}{2}\theta\sigma_{yy}\right)n_y.
\end{aligned} \tag{23}$$

Here, $\mathscr{V}_x = v_x - v_x^W$ is the slip velocity and $P = \rho\theta + \frac{1}{2}\sigma_{yy} - \frac{1}{120}\frac{\Delta}{\theta} - \frac{1}{28}\frac{R_{yy}}{\theta}$. The integrals of f_{R13} over the solid angle, as required in Eq. (14), cannot be solved algebraically, hence we expanded f_{R13} in the non-equilibrium quantities $\{\mathscr{V}_i, \sigma_{ij}, q_i, \ldots\}$ to second order. Note that this is *not* a linearization in the orders of Knudsen number, but in the deviation from equilibrium state. For small lid velocity, as considered here, this deviation is small, hence, it should be sufficient to only consider up to the second order.

From the boundary conditions we can see that, while the isotropically scattering wall is adiabatic, the normal heat flux q_y does not vanish. Indeed, as we expected from Eq. (11), slip friction creates heat that must go into the gas.

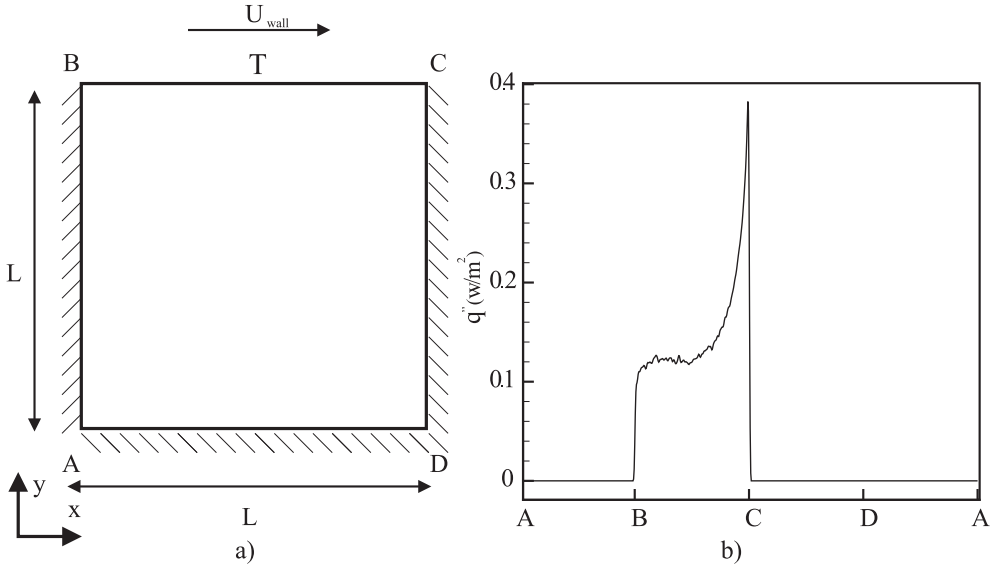

Fig. 2. a) Adiabatic cavity geometry, b) Heat flux through the walls of cavity at $U_{Wall} = 50$ ms^{-1}, Kn = 0.05.

The corresponding slip boundary conditions for the NSF equations can be obtained from the boundary conditions for the R13 Eq. (23) by considering the first order terms in Knudsen number, as [33].

$$v_y = 0,$$
$$\sigma_{xy}^{NSF} = -\sqrt{\frac{2}{\pi\theta}}\left(\rho\theta\mathscr{T}_x + \frac{1}{5}q_x^{NSF}\right)n_y, \tag{24}$$
$$q_y^{NSF} = 0.$$

Note that, since the viscous slip heating is of second order in terms of the Knudsen number, it does not show in the NSF limit, hence $q_y = 0$ at the wall.

3.5. Adiabatic Maxwell surface

Another method for modeling the adiabatic surface is based on the Maxwell boundary conditions. Adiabatic boundaries are achieved by *adjusting* the local wall temperature such that the energy flux vanishes. The particles reflecting from the wall follow the Maxwell distribution,

$$f_W = \frac{\rho^W}{m\sqrt{2\pi\theta^W}^3}\exp\left(-\frac{|c_k - v_k^W|^2}{2\theta^W}\right), \tag{25}$$

where θ^W and v_k^W being the known temperature and velocity of the surface [1]. Moreover, ρ^W must be obtained such that particles do not accumulate at the wall.

Considering the frame of reference in which the wall is at rest, the microscopic velocity of the gas particle is $c_k^W = c_k - v_k^W$ and the velocity distribution function $\bar{f}$ of the gas in an infinitesimal neighborhood of the wall is given by

$$\bar{f} = \begin{cases} f_W, & c_k^W n_k \geq 0 \\ f(c_i^W, x_i, t), & c_k^W n_k \leq 0, \end{cases} \tag{26}$$

where $f(c_k^W, x_k, t)$ is the velocity distribution function in the gas.

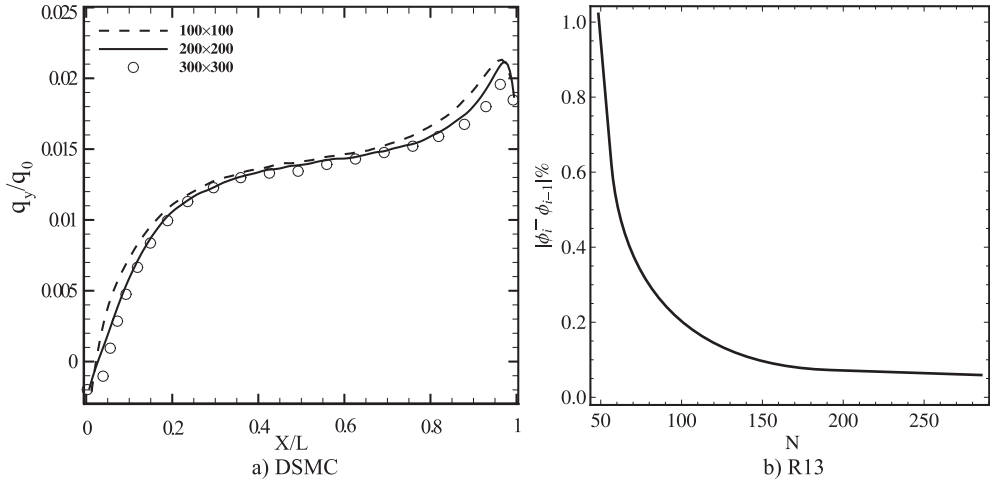

Fig. 3. Grid dependency study test: a) vertical heat flux along the driven lid for DSMC method at Kn = 0.1, b) variation of relative percentage changes in the net heat flux by number of grid points along the driven lid for R13 solution at Kn = 0.1.

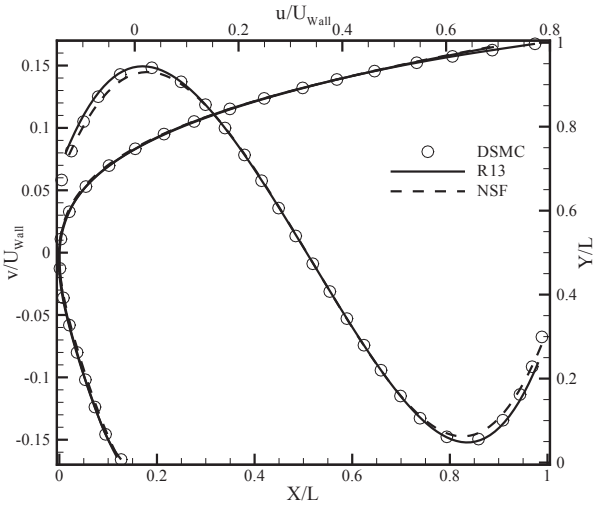

a) Kn=0.05

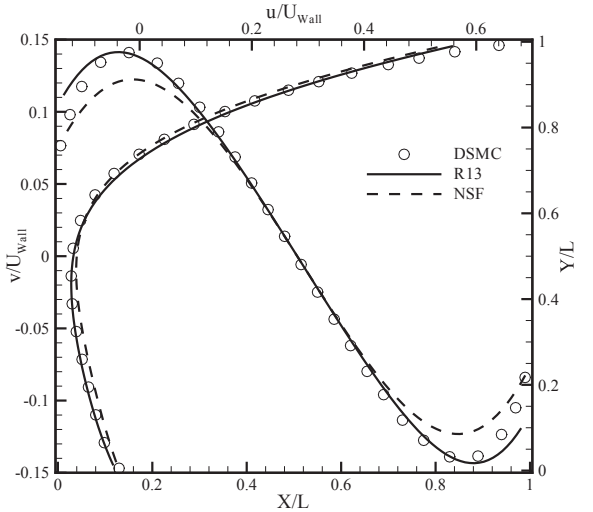

b) Kn=0.1

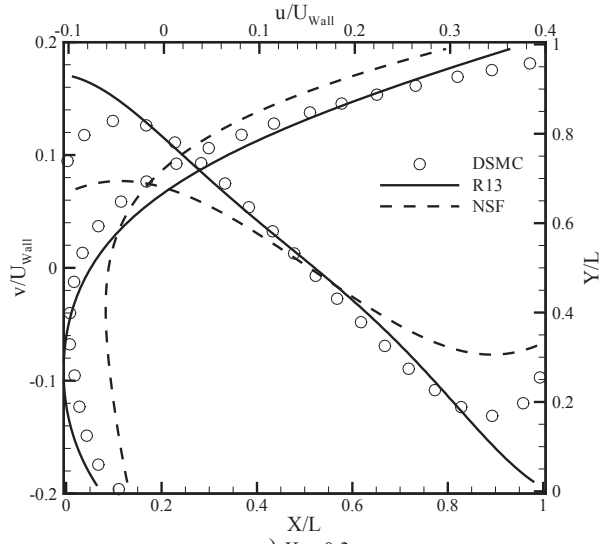

c) Kn=0.3

Fig. 4. Comparison of horizontal and vertical velocity components on the vertical and horizontal centerlines of the cavity for U_{wall} = 50 ms^{-1}, a) Kn = 0.05, b) Kn = 0.1, c) Kn = 0.3.

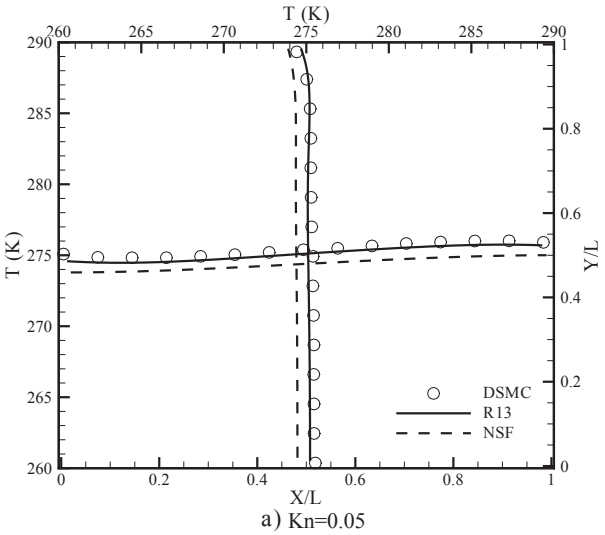

a) Kn=0.05

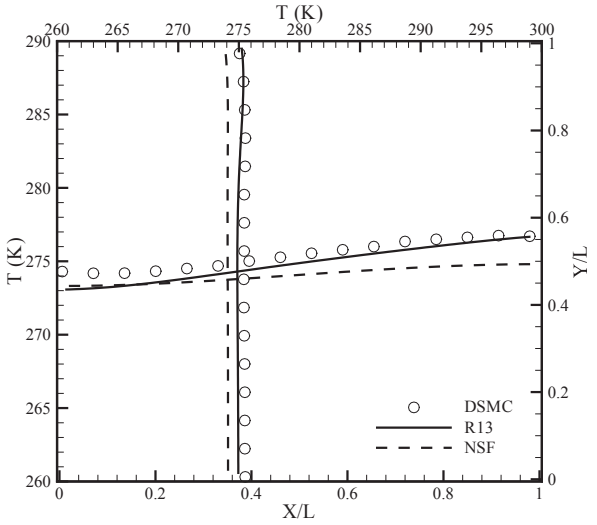

b) Kn=0.1

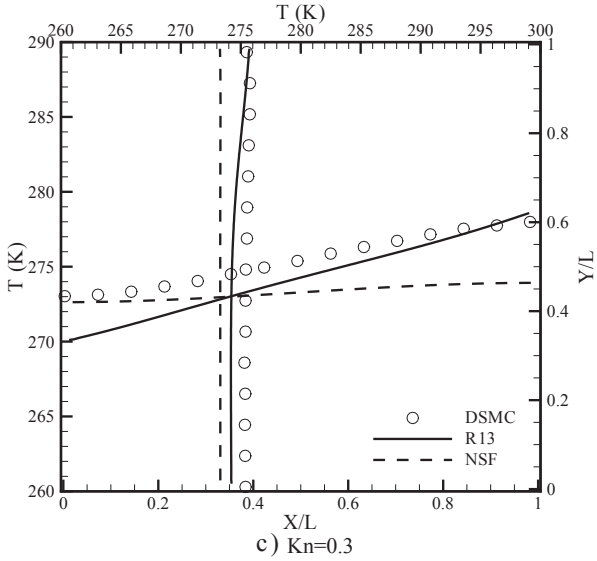

c) Kn=0.3

Fig. 5. Comparison of temperature profiles on the horizontal and vertical centerlines of cavity for U_{wall} = 50 ms^{-1}, a) Kn = 0.05, b) Kn = 0.1, c) Kn = 0.3.

Inserting the distribution function (20) and performing the integration in Eq. (19) for the Maxwell model Eq. (26) leads to the wall-boundary conditions [11].

$$
\begin{aligned}
&v_y = 0,\\
&\sigma_{xy} = \sqrt{\frac{2}{\pi\theta}}\left(-P\mathscr{V}_x - \frac{1}{5}q_x - \frac{1}{2}m_{xyy}\right)n_y,\\
&q_y = \sqrt{\frac{2}{\pi\theta}}\left(-2P\mathscr{T} + \frac{1}{2}P\mathscr{V}_x^2 - \frac{1}{2}\theta\sigma_{yy} - \frac{1}{15}\Delta - \frac{5}{28}R_{yy}\right)n_y,\\
&R_{xy} = \sqrt{\frac{2}{\pi\theta}}\left(P\theta\mathscr{V}_x - \frac{11}{5}\theta q_x - \frac{1}{2}\theta m_{xyy} - P\mathscr{V}_x^3 + 6P\mathscr{V}_x\mathscr{T}\right)n_y,\\
&m_{xxy} = \sqrt{\frac{2}{\pi\theta}}\left(-\frac{1}{14}R_{xx} - \theta\sigma_{xx} + \frac{1}{5}\theta\sigma_{yy} - \frac{1}{5}P\mathscr{T} + \frac{4}{5}P\mathscr{V}_x^2 - \frac{1}{150}\Delta\right)n_y,\\
&m_{yyy} = \sqrt{\frac{2}{\pi\theta}}\left(\frac{2}{5}P\mathscr{T} - \frac{3}{5}P\mathscr{V}_x^2 - \frac{7}{5}\theta\sigma_{yy} + \frac{1}{75}\Delta - \frac{1}{14}R_{yy}\right)n_y.
\end{aligned}
\tag{27}
$$

Here, $\mathscr{T} = T - T_W$ denotes the temperature jump. In order to obtain the adiabatic boundary condition from the Maxwell boundary equations, we have to adjust the heat flux to mimic the no energy transfer condition, Eq. (11), and set $q_y = -\mathscr{V}_x\sigma_{xy}$, to account for the viscous slip heating. The temperature jump corresponding to the adiabatic fully diffusive Maxwell surface is obtained from $(27)_3$ as

$$
\begin{aligned}
\mathscr{T} = T - T_W = &-\frac{1}{4}\frac{\theta\sigma_{yy}}{P} - \frac{1}{30}\frac{\Delta}{P} - \frac{5}{56}\frac{R_{yy}}{P} + \frac{1}{4}\mathscr{V}_x^2\\
&-\frac{1}{4}\frac{m_{xyy}V_x}{P} - \frac{1}{10}\frac{q_x\mathscr{V}_x}{P}.
\end{aligned}
\tag{28}
$$

By substituting the corresponding wall temperature, T_W, into the Maxwell boundary conditions for the diffusive wall (27), we obtain *the same* boundary conditions for the isotropically scattering adiabatic surface, Eq. (23).

The above calculation shows that whether we adjust the temperature of the surface to get adibaticity at the wall, or use the isotropic scattering kernel to obtain the corresponding macroscopic boundary condition, the results, at least on the level of R13 equations, are the same. Both models lead to the adiabatic surface. However, adjusting the temperature in the microscopic DSMC model leads to an iterative scheme. The wall temperature should be modified for each iteration so that the final temperature distribution on the wall can mimic the no-energy-transfer from the surface. On the other hand, if we use the isotropic scattering kernel, there is no need to prescribe the temperature, and the wall temperature will be obtained accordingly.

We also note that the proposed method of modeling the adiabaticity using the isotropic scattering kernel is more consistent with the underlying physics of light gas particles interacting with heavy surface particles outlined in Section 3.1. The adiabatic Maxwell surface is a well-working model, however, the complexity in nature of this wall, i.e., adjusting the temperature of each individual surface element, seems rather unphysical.

4. Results and discussion

4.1. Micro lid driven cavity

We consider the partly adiabatic two-dimensional lid driven micro cavity, depicted in Fig. 2-a and compare the DSMC, R13 and NSF results in rarefaction regime. All walls except for the driven lid are assumed to be adiabatic; the top wall is fully diffusive and

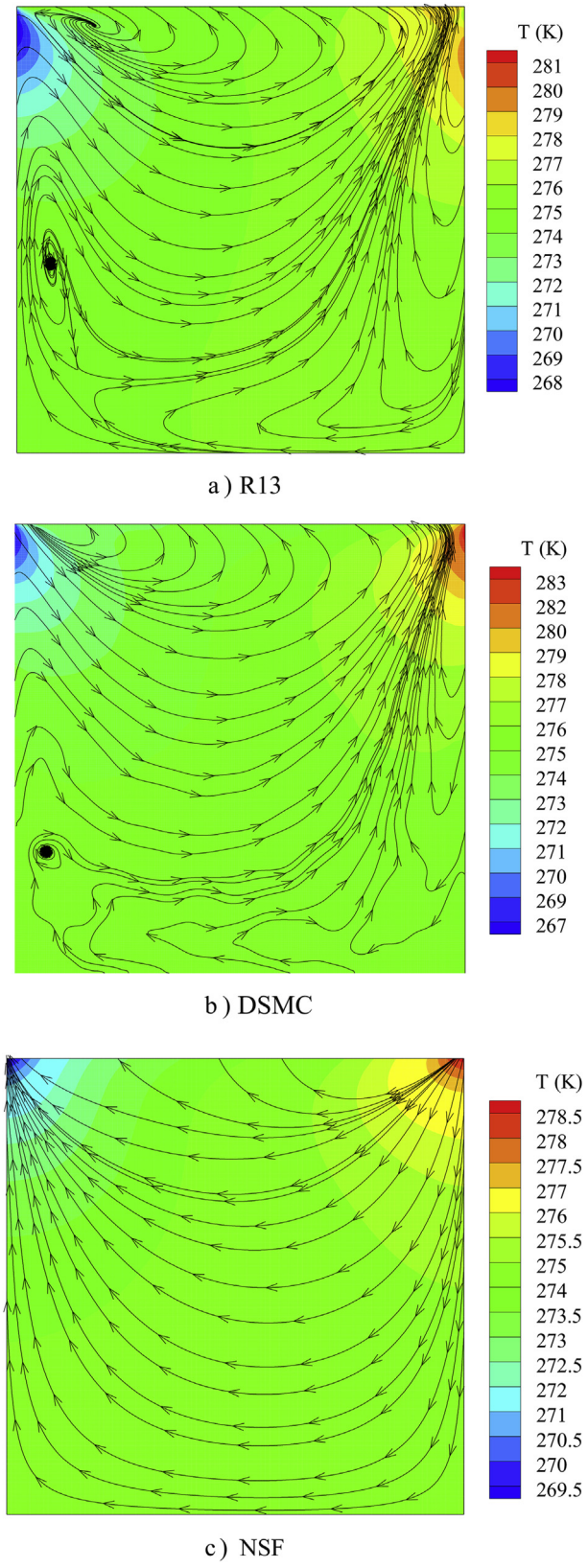

Fig. 6. Heat flux streamlines and temperature contour inside the cavity at Kn = 0.05, a) R13, b) DSMC, c) NSF.

isothermal at $T = 273$ K. The corresponding boundary conditions for a fully diffusive surface in DSMC and R13 equations are well studied and can be found in Ref. [34]. This geometry serves as a test for the implementation of the adiabatic boundary conditions (18) for DSMC and (23) for R13 equations. The top lid velocity is $U_{Wall} = 50$ ms^{-1} and the computations are done for Knudsen numbers Kn = 0.05, 0.1, 0.3. The side length of the cavity walls is fixed at $L = 1$ μm and rarefaction occurs due to the reduction of the pressure in the cavity.

Fig. 2-b shows the heat flux variation for the DSMC results along the four walls of cavity when $U_{Wall} = 50$ ms^{-1} and Kn = 0.05. The heat flux of the monatomic rarefied flow through the walls is obtained by

$$q'' = \frac{B \times m}{2 \times N \times t} \sum_{i=1}^{N} \frac{\left[\left(c_x'^2 + c_y'^2 + c_z'^2\right)_i - \left(c_x^2 + c_y^2 + c_z^2\right)_i\right]}{A_i}.$$

Here, B is the number of real gas molecules represented by each DSMC particle, N is the number of particle-surface collisions taking place in the process of sampling, t is the elapsed time in the sampling, and A is the area of the cell through which the particle transfer energy to the surface.

Fig. 2-b demonstrates that the adiabatic boundary condition Eq. (18), for DSMC indeed guarantees the full adiabaticity on the fixed walls. This is not so in Refs. [16,18], where adiabaticity is implemented by an iterative scheme that sets the local boundary temperature such that the local heat flux into the wall vanishes; as a result, one observes oscillation of heat flux on the walls. We emphasize that by following the methodology in the current study, as one sets a surface to be adiabatic by isotropic scattering, there is no need to prescribe any temperature for the wall. We also note that the iterative schemes are less exact, and more time consuming. To us, the modelling of an adiabatic surface by isotropic scattering appear more natural.

4.2. Grid dependency

In order to perform the grid dependency test for DSMC, we use three grids composed of 100 × 100, 200 × 200 and 300 × 300 cells, and compare the heat flux profile along the driven lid, when $U_{Wall} = 100$ ms^{-1} and Kn = 0.1. Figure 3-a demonstrates that the results for 200 × 200 and 300 × 300 are numerically equivalent, while the 100 × 100 grid gives insufficient results; therefore we used 200 × 200 grid cells for the following results.

To determine an appropriate mesh size for the R13 solution, a grid dependency test was conducted as well. Since solving the macroscopic transport equations takes considerable less amount of time than the DSMC approach, various meshes of size $N = 40$, 50, 100, 200, 400 were tested. For these cases the relative percentage changes in the net heat flux along the driven lid was monitored as the grid was refined successively, in Fig. 3-b. It is evident that the relative percentage change in the net heat flux between two successive grid sizes is less then 0.2% as the grid is refined beyond 100 × 100. Therefore, for the following R13 results the grid with 100 × 100 cells is used.

It is also worth noting that a typical simulation with the R13 equations (as well as NSF) with a grid size of 100 × 100 takes about 20 min on a single quad core desktop PC. Whereas, depending on the flow parameters and the value of the Knudsen number, the corresponding DSMC simulation takes up to 70 h of the computational time.

4.3. Velocity profile

Figure 4 shows the velocity components on two centerlines of the cavity for $U_{wall} = 50$ ms^{-1} in the rarefied regime. For the small Knudsen number (Kn = 0.05) the three approaches– DSMC, R13 and NSF equations predict the same results for the velocity. As the Knudsen number increases we observe a deviation in the results of the continuum approaches from the molecular method; however, the predicted results of the R13 method are in better agreement with DSMC data, as compared to NSF.

A closer look into Fig. 4-c shows that the largest deviation in the predicted velocity by R13 from the DSMC solution takes place in the Knudsen layer, in the vicinity of the side walls. Note that in this rarefaction regime the Knudsen layer almost covers the entire flow field. The R13 equations, by benefiting from the Knudsen layer terms, can provide an approximation to the Knudsen layer, however, in the presence of large non-equilibrium effects this approximation becomes less accurate. The NSF equations, on the other hand, do not include the Knudsen layer terms at all and their results deviates from the DSMC solution, almost in the entire domain in Fig. 4-c.

4.4. Temperature profile

Variation of the flow temperature on the centerlines of the cavity with $U_{wall} = 50$ ms^{-1} is depicted in Fig. 5. This figure

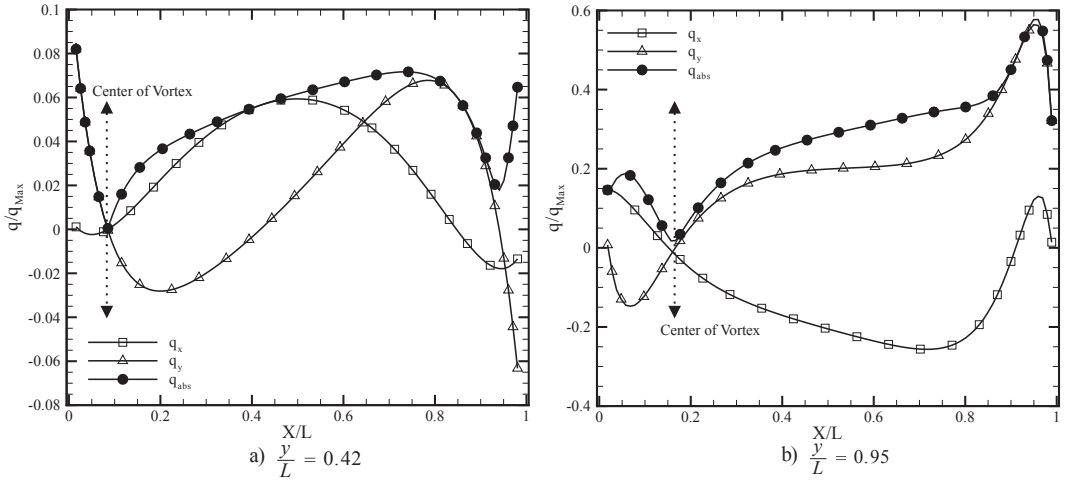

Fig. 7. Component of the relative heat flux vector across the two vortices for R13 results, a) $Y/L = 0.42$, b) $Y/L = 0.95$.

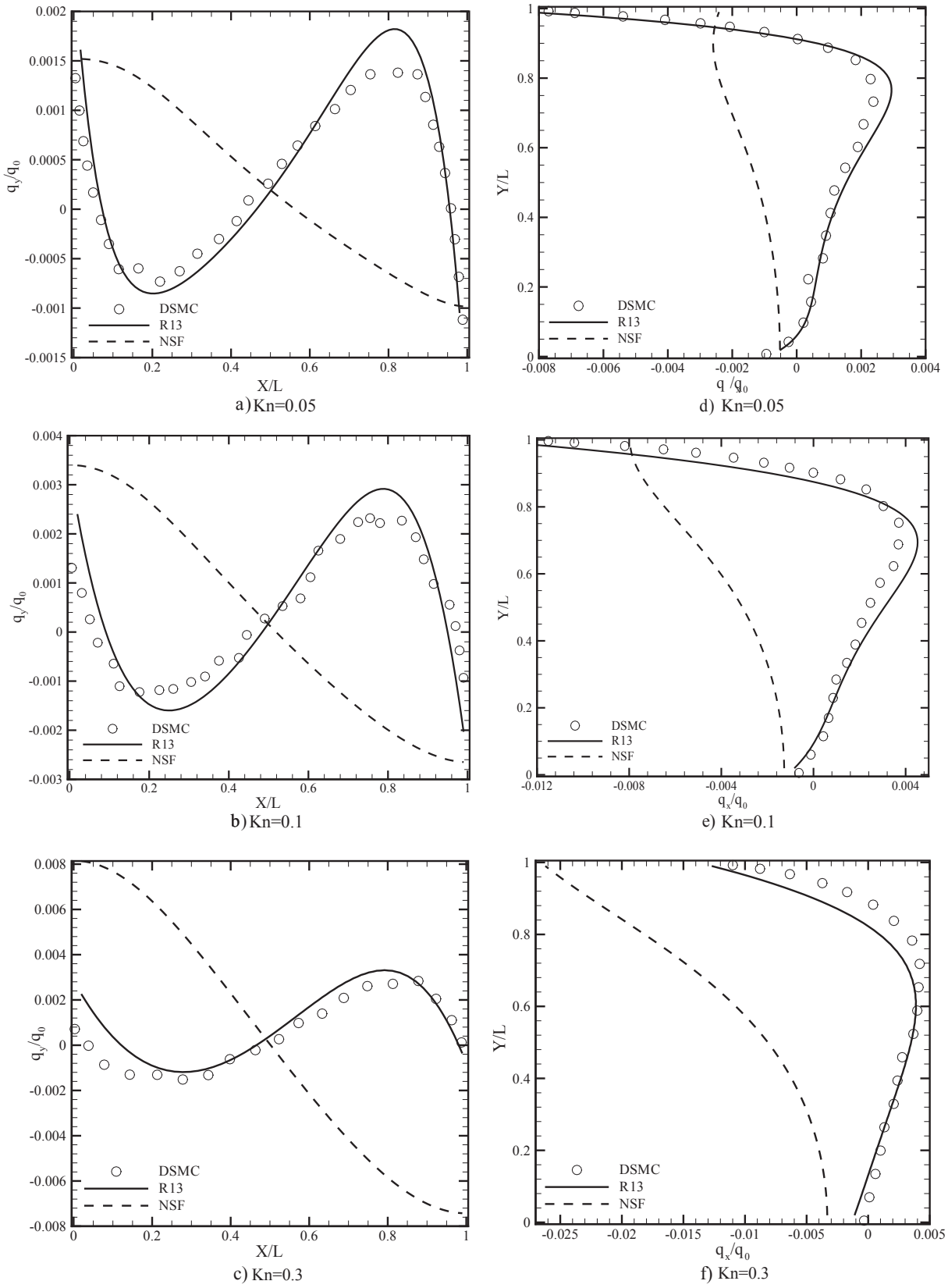

Fig. 8. Heat flux over the centerlines of the cavity, a&d) Kn = 0.05, b&e) Kn = 0.1, c&f) Kn = 0.3.

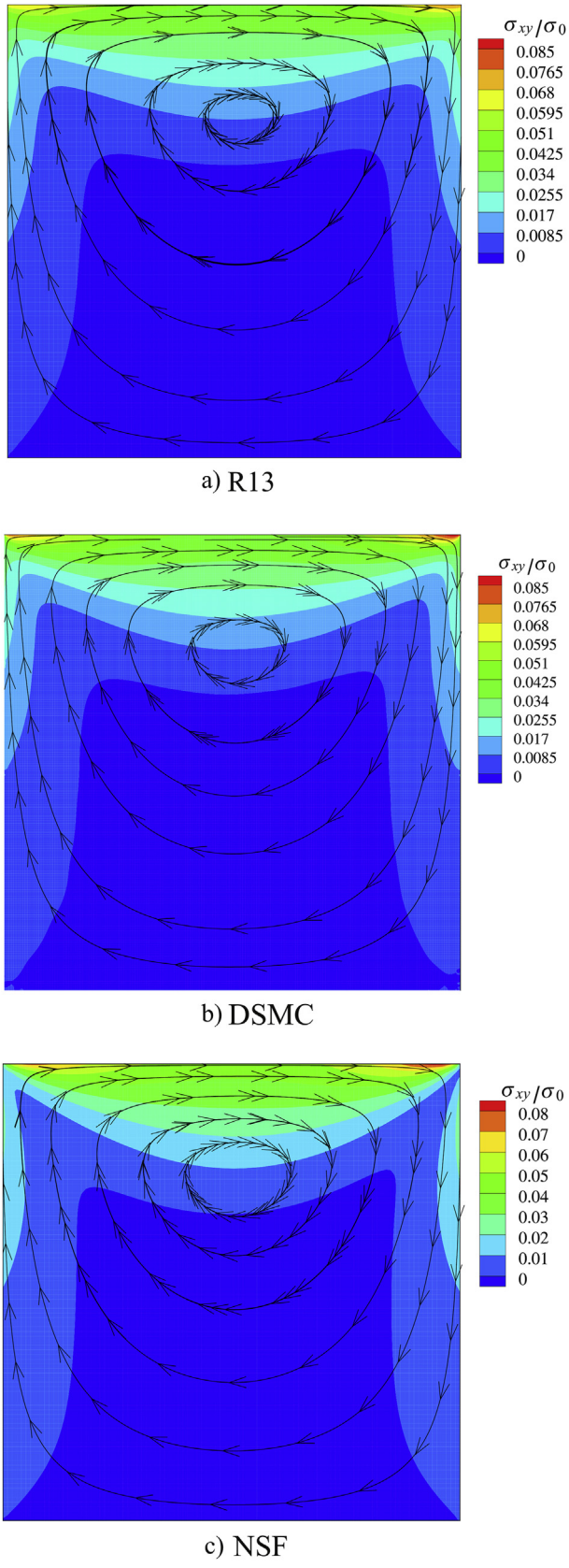

Fig. 9. Velocity streamlines and shear stress contour for U_{Wall} = 50 ms^{-1} and Kn = 0.05, a)R13, b)DSMC, c)NSF.

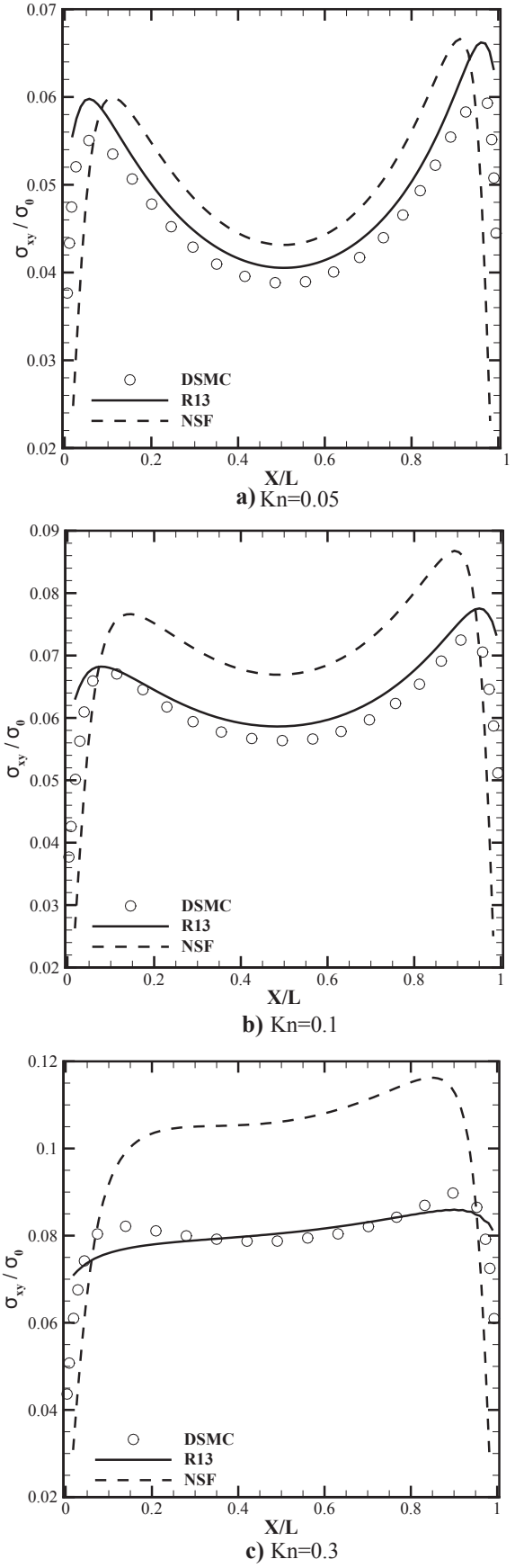

Fig. 10. Comparison of shear stress along the driven lid of the cavity: a) Kn = 0.05, b) Kn = 0.1, c) Kn = 0.3.

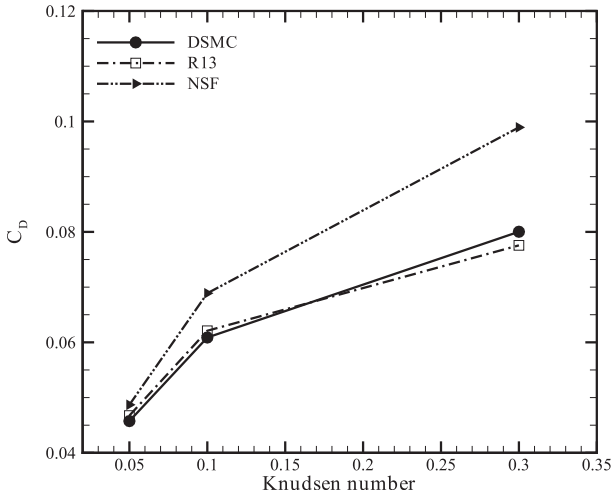

Fig. 11. Comparison of the drag coefficient obtained from the three methods.

illustrates that up to Kn = 0.1, the R13 equation can accurately predict the temperature variation along the two centerlines. As Knudsen number increases, the R13 equations slightly underpredict the flow temperature (less than 1%) in close vicinity of the left adiabatic wall. As shown in Fig. 5, the flow temperature increases and decreases near the right and left walls, respectively. As the rarefied flow approaches the right wall, it undergoes a compression which subsequently increases the flow temperature. The R13 equations can capture the increase and decrease of the flow temperature close to the side walls with a slight difference in the temperature magnitude in the non-equilibrium regime.

4.5. Heat flux; viscous slip heating

4.5.1. Heat lines

Fig. 6 shows the heat flux streamlines inside the cavity for the three approaches when Kn = 0.05. Similar to the case of a cavity with isothermal wall [23], the unconventional "cold-to-hot" heat transfer is observed. By using the macroscopic equations, Rana et al. [27] showed that this so called anti-Fourier heat flux is due to domination of the non-dimensional shear stress gradient over the temperature gradient. For a more detailed description of this rarefaction effect see Ref. [27].

A closer look into the DSMC and R13 results shows that the associated curved structures of the heat flux lines are properly captured by the macroscopic method. More interestingly, the DSMC and R13 results show heat apparently leaving the adiabatic surface while this effect is not observed in NSF. This heat is not coming from the walls, but created in the slip layer by friction.

In fact, the particles in the cell adjacent to the adiabatic surfaces collide with each other (and not the surface), which subsequently leads to viscous heat generation in the boundary cells. This heat cannot escape into the adiabatic wall; consequently, it will be directed towards the gas. Figure 6-a demonstrates that the R13 equations also predict the viscous heat generation at the boundaries due to the rarefaction effects. In fact, Eq. (23) shows that the normal component of the heat flux in the proximity of the adiabatic surface, is the product of slip velocity and shear stress at the boundary, i.e., $q_y = -\sigma_{xy}\mathscr{V}_x$.

Comparison of the heat lines for the R13 and DSMC results also shows the appearance of a heat flux vortex in the bottom left, and a heat source in the top left side of the cavity. Figure 7 shows the heat flux profile along the two horizontal lines passing through the centre of bottom vortex, $Y/L = 0.42$, and the top source at $Y/L = 0.95$ for R13 results. The maximum value of heat flux in the entire domain ($q_{max} = 0.0187$) is used to non-dimensionalize the heat flux components. Figure 7-a demonstrates that the absolute value of the heat flux vector becomes zero at the center of the bottom vortex, which consequently leads to circulation of the heat lines around it. Note that the DSMC solution for heat flux lines in this region suffers markedly from large noises. Figure 7-b illustrates that the heat source on the top left corner appears due to the very small value of absolute heat flux in this region.

4.5.2. Heat flux along the centerlines

Comparison of the heat flux profiles along the two centerlines of the cavity is depicted in Fig. 8. This figure illustrates that the R13 equations can accurately predict the values of heat flux along the two centerlines in the adiabatic cavity. In addition, Fig. 8 shows that increasing the rarefaction effects, i.e., larger Knudsen number, enlarges the heat flux magnitude predicted by the NSF equations

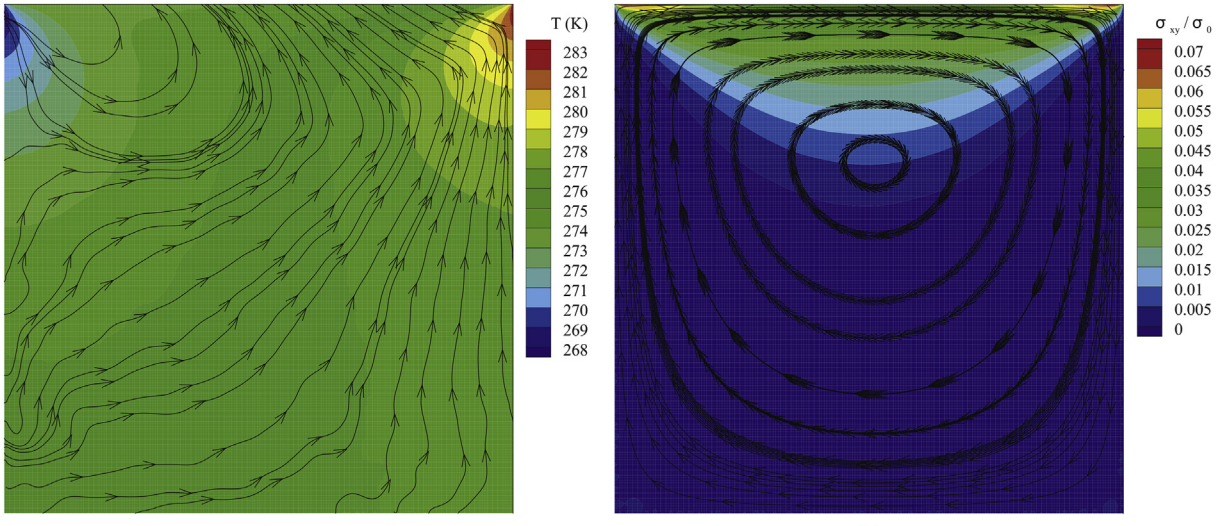

Fig. 12. Flow formation predicted by DSMC inside a lid driven cavity with three specular walls and diffusive driven lid, $U_W = 50\frac{m}{s}$, Kn = 0.05. a) Heat flux streamlines overlaid on the temperature distribution, b) Velocity streamlines overlaid on the shear stress distribution.

notably; however, the heat flux magnitude predicted by the R13 method is not significantly increased over the Knudsen regime. The small increment of the vertical heat flux over the horizontal centerlines for R13 results can be due to small increment role of the Knudsen layer as well as the third order terms in the heat flux governing equation, Eq. (7).

4.6. Shear stress

4.6.1. Shear stress distribution

Figure 9 shows the shear stress distribution overlaid on the velocity streamlines, when Kn = 0.05 for the three methods of solution. The shear stress is nondimensionlized with respect to $\sigma_o = \rho_0 R T_0$. The R13 equations can accurately predict the shear stress distribution inside the cavity; however, NSF predict a different distribution inside the flow field.

4.6.2. Shear stress on the driven lid

In order to investigate the accuracy of the employed methods in more detail, we illustrate the shear stress profile along the driven lid in Fig. 10. The R13 equations provide very accurate results for the magnitude of the shear stress in the vicinity of driven lid. As the lid velocity increases, the shear stress in the flow field enlarges. A closer look into Fig. 10 shows that the value of the shear stress predicted by R13 is in maximum deviation from the DSMC results around the two top corners of the cavity, where the flow undergoes sudden changes. In this region the local Knudsen number is significantly larger than the global Knudsen number, which indeed limits the accuracy of the shear stress equation close to the top corners.

4.6.3. Drag coefficient

Although the R13 equations do not fully predict the accurate local values, they describe the overall behavior of the flow rather well. Therefore, we were encouraged to determine the R13 drag coefficient and compare it with the DSMC results. The drag coefficient on the driven lid is obtained by

$$C_D = \frac{\int_0^L \sigma_{xy} dx}{\sigma_0 L}$$

Figure 11 shows the variation of the drag coefficient with the Knudsen number. Comparison of the R13 results with the DSMC data demonstrates that the R13 equations can accurately predict the drag coefficient up to Kn = 0.3. This figure is a good indicator of the strength of the R13 equations, when it comes to predicting the global flow behaviors.

4.7. Cavity with specular reflecting walls

Another method to model the adiabaticity of the surface is to use the specular reflection kernel. In this method, the process of particle surface collision guaranties no-energy-transfer through the wall, however, the gas undergoes a perfect slip condition at the surface. Figure 12 shows the DSMC results for the lid driven cavity with 3 specular walls. The top driven lid is assumed to be a diffusive reflector at $T = 273\ K$.

Fig. 12-a shows the heat flux streamlines overlaid on the temperature distribution. Compared to Fig. 6-b, a similar range of temperature is predicted inside the domain. However, the heat lines are completely different. More interestingly, the shear stress distribution, Fig. 12-b, shows a rather large shear stress close to the top lid, while the rarefied flow in the rest of the domain exhibits small shear stress. The perfect slip condition on the wall leads to a very small shear stress distribution inside the flow field. Since the assumption of the perfectly smooth surface at the microscopic level, specular reflection, is not realistic, such modelling of adiabaticity is not of our interest.

5. Conclusion

In the current study microscopic and macroscopic models are employed to model adiabatic surfaces. When a gas with light particles interacts with a rough surface of heavy particles, the gas–surface interaction can be considered adiabatic, and the reflecting particles have no preference in the reflection direction (isotropic scattering). In the DSMC method the isotropic scattering kernel is utilized to ensure the no-energy-transfer condition on each particle colliding with the adiabatic surface. The corresponding macroscopic boundary equations for the isotropic scattering distribution functions are obtained for the R13 equations. By taking into account the second order nonlinearity in the normal heat flux to an adiabatic surface, the viscous slip heating effect appears. The generation of heat due to intermolecular collision in the adjacent cell to the adiabatic surface (microscopic approach) can be well captured, and interpreted, by the product of the slip velocity and the shear stress on the adiabatic wall (macroscopic approach). The viscous slip heating that occurs at all slip boundaries can be more clearly identified in the case of adiabatic surface. Comparison of the solution for temperature, shear stress and heat flux profiles obtained from R13 and DSMC methods demonstrates the capability of the R13 equations in predicting the flow behaviors upto Kn = 0.3.

To be more general, the reflection of a particle from a surface can be modeled as a superposition of the diffusive reflection, specular reflection and isotropic scattering [32]. Therefore, using a general reflection kernel for the particle based method, which can model the three possible scenarios, seems to be essential.

Acknowledgement

This research was supported by the Natural Sciences and Engineering Research Council NSERC (411974-2011).

References

[1] C. Cercignani, Theory and application of the Boltzmann equation, Scottish Academic Press, 1975.
[2] F.M. Sharipov, E.A. Subbotin, On optimization of the discrete velocity method used in rarefied gas dynamics, ZAMP 44 (1993) 572–577.
[3] D. Valougeorgis, S. Naris, Acceleration schemes of the discrete velocity method: gaseous flows in rectangular microchannels, SIAM J. Sci. Comput. 25 (2003) 534–552.
[4] H. Grad, On the kinetic theory of rarefied gases, Commun. Pure Appl. Math. 2 (1949) 331.
[5] W. Weiss, Continuous shock structure in extended thermodynamics, Phys. Rev. E 52 (1995) 5760.
[6] M. Torrilhon, H. Struchtrup, Regularized 13-moment equations: shock structure calculations and comparison to Burnett models, J. Fluid. Mech. 513 (2004) 171–198.
[7] H. Struchtrup, Scaling and expansion of moment equations in kinetic theory, J. Stat. Phys. 125 (2006) 565.
[8] H. Struchtrup, M. Torrilhon, Regularized 13 moment equations for hard sphere molecules: linear bulk equations, Phys. Fluids 25 (2013) 052001.
[9] H. Struchtrup, M. Torrilhon, Regularization of Grad's 13–moment equations: derivation and linear analysis, Phys. Fluids 15 (2003) 2668.
[10] H. Struchtrup, M. Torrilhon, H-theorem, regularization, and boundary conditions for linearized 13–moment equations, Phys. Rev. Lett. 99 (2007) 014502.
[11] M. Torrilhon, H. Struchtrup, Boundary conditions for regularized 13–moment–equations for micro–channel flows, J. Comp. Phys. 227 (2008) 1982.
[12] G.A. Bird, Molecular gas dynamics and the direct simulation of gas flows, Oxford University Press, 1994.
[13] W. Wagner, A convergence proof for Bird's Direct Simulation Monte Carlo method for the Boltzmann equation, J. Stat. Phys. 66 (1992) 1011.
[14] J. Maxwell, On stresses in rarified gases arising from inequalities of temperature, Philos. Trans. R. Soc. 170 (1879) 231–256.

[15] J.J. Hinchen, W. Foley, Rarefied gas dynamics, Academic Press, New York, 1966.
[16] Q.W. Wang, C.L. Zhao, M. Zeng, Y.N. Wu, Numerical investigation of rarefied diatomic gas flow and heat transfer in a microchannel using DSMC with uniform heat flux boundary condition-part I: numerical method and validation, Numer. Heat. Tr-B 53 (2008) 160–173.
[17] Q. Wang, X. Yan, Q. He, Heat-flux-specified boundary treatment for gas flow and heat transfer in microchannel using direct simulation monte carlo method, Int. J. Numer. Meth. Engng. 74 (2008) 1109–1127.
[18] H. Akhlaghi, E. Roohi, S. Stefanov, A new iterative wall heat flux specifying technique in DSMC for heating/cooling simulations of mems/nems, Int. J. Therm. Sci. 59 (2012) 111–125.
[19] P. Tzeng, C. Soong, M. Liu, T. Yen, Atomistic simulation of rarefied gas natural convection in a finite enclosure using a novel wall-fluid molecular collision rule for adiabatic solid walls, Int. J. Heat Mass Transf. 51 (34) (2008) 445–456.
[20] T. Klinc, I. Kuščer, Slip coefficients for general gas surface interaction, Phys. Fluids 15 (1972) 10118.
[21] E. Roohi, M. Darbandi, V. Mirjalili, Direct Simulation Monte Carlo solution of subsonic flow through micro/nanoscale channels, J. Heat. Transf. 131 (2009) 92402.
[22] M. Darbandi, E. Roohi, DSMC simulation of subsonic flow through nanochannels and micro/nano steps, Int. Commun. Heat. Mass 38 (2011) 1444–1449.
[23] A. Mohammadzadeh, E. Roohi, H. Niazmand, S. Stefanov, R.S. Myong, Thermal and second-law analysis of a micro- or nanocavity using direct-simulation Monte Carlo, Phys. Rev. E 85 (2012) 056310.
[24] A. Mohammadzadeh, E. Roohi, H. Niazmand, A parallel DSMC investigation of monatomic/diatomic gas flow in micro/nano cavity, Num. Heat. Trans. Part A Appl. 63 (2013) 305–325.
[25] H. Niazmand, A. Mohammadzadeh, E. Roohi, Predicting continuum breakdown of rarefied micro/nano flows using entropy and entropy generation analysis, Int. J. Mod. Phys. C 24 (2013), 1350029–1350029.
[26] H. Struchtrup, Macroscopic transport equations for rarefied gas flows: Approximation methods in kinetic theory, Springer, 2005.
[27] A.S. Rana, M. Torrilhon, H. Struchtrup, A robust numerical method for the R13 equations of rarefied gas dynamics: application to lid driven cavity, J. Comp. Phys. 236 (2012) 169.
[28] H. Grad, Principles of the kinetic theory of gases, in: Handbuch der Physik, vol. 12, Springer, Berlin, 1958.
[29] G.M. Kremer, An introduction to the Boltzmann equation and transport processes in gases, Springer, 2010.
[30] Y. Sone, Kinetic theory and fluid dynamics, Birkhäuser, Boston, 2002.
[31] L. Thomas, In fundamental of gas-surface interactions, Academic Press, New York, 1967.
[32] H. Struchtrup, Maxwell boundary condition and velocity dependent accommodation coefficient, Phys. Fluids 25 (2013) 112001.
[33] H. Struchtrup, M. Torrilhon, Higher-order effects in rarefied channel flows, Phys. Rev. E 78 (2008) 046301.
[34] A.S. Rana, A. Mohammadzadeh, H. Struchtrup, A numerical study of the heat transfer through a rarefied gas confined in a micro cavity, Cont. Mech. Thermodyn. 27 (2015) 433–446.